Int J Fract (2022) 235:159–178
https://doi.org/10.1007/s10704-022-00647-x

ORIGINAL PAPER

In-situ dwell-fatigue fracture experiment and CPFE simulation of SLM AlSi10Mg alloy at high temperature

Zhen Wang · Chong Zhao · Jie Wang · Wenwang Wu · Xide Li

Received: 2 January 2022 / Accepted: 10 May 2022 / Published online: 20 June 2022

Abstract The creep-fatigue fracture behavior of selective laser melting (SLM) AlSi10Mg alloy was studied by conducting in-situ scanning electron microscopy experiments at 500 °C. Dwell times of 0, 60 and 120 s were introduced to the tensile-tensile fatigue. The experimental results indicated that the lifetime decreased with lengthening of the dwell time from 0 to 120 s, which closely related to the deformation response behavior of the material. The process of the fracture evolution of the alloy was characterized and analyzed using in-situ scanning electron microscopy images and the fracture morphology. The creep-fatigue fracture mechanism of SLM AlSi10Mg alloy was revealed. Finally, combined with crystal plasticity finite element simulation, the Mises stress, plastic strain and elastic stored energy were used to explain the crack nucleation of SLM AlSi10Mg alloy under fatigue and dwell-fatigue.

Keywords SLM AlSi10Mg alloy · Fatigue and dwell-fatigue · Crystal plasticity finite element · High temperature · Crack nucleation

1 Introduction

Compared with the traditional manufacturing of structural components, additive manufacturing (AM) is more economic and provides more freedom in designing the shape of structural components. A popular technology for the AM of metal materials is selective laser melting (SLM). The components made adopting SLM have a dense and homogeneous fine-grain microstructure, which provides SLM-made materials great advantages in terms of their mechanical properties even when compared with traditional casting materials (Yan et al. 2020). Owing to the good processing ability and high specific strength of Al-Si alloys, the SLM AlSi10Mg alloy is currently one of the most extensively used alloys in applications of lightweight structures, such as automotive and aerospace structures (Dursun and Soutis 2014). However, structural components are often used in high-temperature environments, and it is thus important to evaluate the high-temperature mechanical

Zhen Wang and Chong Zhao have contributed equally to this work.

Z. Wang · C. Zhao · J. Wang · X. Li (✉)
Department of Engineering Mechanics, Tsinghua University, Beijing 100084, China
e-mail: lixide@tsinghua.edu.cn

Z. Wang
State Key Laboratory for Nonlinear Mechanics (LNM), Institute of Mechanics, Chinese Academy of Sciences, Beijing 100190, China

W. Wu
Institute of Advanced Structure &Technology, Beijing Institute of Technology, Beijing 100081, China

behaviors of SLM AlSi10Mg alloy. Usually, fatigue and the high-temperature creep are the main reasons for the failure of structural components. Although researchers have done much work on the mechanical behaviors of SLM AlSi10Mg alloy, there remains a lack of understanding of the relationship among manufacturing parameters, the microstructure evolution and mechanical properties (Tang and Pistorius 2017, 2019; Paoletti et al. 2021; Uzan et al. 2018; Michi et al. 2021), especially under complex creep-fatigue interaction.

In contrast with the case for traditional casting, pores created in the manufacturing process are the main factor affecting the properties of SLM AlSi10Mg alloy. Aboulkhair et al. (2014) systematically summarized the main factors affecting material properties in SLM technology as the scanning laser power, scanning parameters, powder quality and temperature, with each factor having a variety of subfactors. Many researchers have reduced the porosity of SLM AlSi10Mg alloy by combining manufacturing parameters (Liu et al. 2010; Read et al. 2015; Wu et al. 2020). They have proposed using a laser energy density to correlate the porosity of SLM AlSi10Mg alloy, where the laser energy density is affected by the laser input power, scanning speed, scanning layer thickness, and scanning spacing. Selecting the optimal laser energy density corresponding to the minimum porosity only reduces and does not eliminate the porosity of SLM AlSi10Mg alloy. In addition, post-treatment methods have been used to reduce the porosity and improve the fatigue properties of SLM AlSi10Mg alloy. Brandl (2012) and Schnerller (2019) respectively reduced the porosity of SLM AlSi10Mg alloy adopting T6 and hot-isostatic-pressing heat treatments. Experimental tests suggested that both treatments improve fatigue properties. It was found that the hot-isostatic-pressing heat treatment greatly reduces the porosity and maximum pore size of a material, and the change in microstructure was consistent with that of the T6 treatment. Meanwhile, Zhang et al. (2018) found that three heat treatment methods worsened the fatigue properties of SLM AlSi10Mg alloy. The worsening of the properties was mainly due to damage to the Si network structure in SLM AlSi10Mg alloy during the heat treatments. In conclusion, although porosity can be reduced by adjusting the manufacturing parameters and applying a post treatment, micropore defects inevitably remain in the SLM AlSi10Mg alloy. Additionally, progress has been made in the study of the effect of porosity on fatigue life but there remains a lack of research on the mechanism by which pores affect the fatigue life and crack growth behaviors. This is mainly because macroscale high-temperature experiments cannot observe the microstructural evolution and the interaction of micropores and small cracks for SLM AlSi10Mg alloy.

Conducting an in-situ observation experiment is a powerful way of studying the mechanical properties associated with the microstructure of materials. Zhao et al. (2019) carried out an in-situ tensile study of SLM AlSi10Mg alloy at room temperature. They observed crack propagation in real time and discovered the phenomenon of microcracks traversing the molten pool boundary. Xu et al. (2021) studied the fatigue properties and crack propagation behavior of SLM AlSi10Mg with different building directions at room temperature using an in-situ scanning electron microscope (SEM) platform. Their experimental results showed that the fatigue performance in the melted pool was better than that at the boundary of the melted pool, and the difference led to different fatigue crack growth behaviors for different building directions. However, there is no relevant report on the effect of pores produced in the manufacturing process on the crack growth behavior under high creep fatigue. Adopting in-situ synchrotron tomography technology, Bao et al. (2020) studied the pore structure evolution and fracture characteristics of SLM AlSi10Mg alloy at room temperature and 250 °C under ultra-low cycle fatigue. Their results showed that the pores gradually elongated with an increase in the number of fatigue cycles at 250 °C. The crack nucleated from the inside to the outside, and ductile fracture then occurred. Michi et al. (2021) in their review pointed out that SLM AlSi10Mg alloy is expected to be applied at higher temperature to realize a lightweight structure. Therefore, our group carried out in-situ fatigue experiments from room temperature to 600 °C for test pieces with different laser scanning speeds and observed the interaction between the crack growth and pores in real time. The experimental results showed that a higher experimental temperature and higher porosity resulted in a higher crack growth rate (Wang et al. 2019). For SLM AlSi10Mg alloy, existing research results are

limited to the exploration of the microstructure evolution and crack propagation behavior under a fatigue condition. However, as an important engineering structural material, AlSi10Mg alloy should undergo not only cyclic loading but also stable loading periods at high temperature, leading to creep-fatigue interaction. To the authors' knowledge, few studies have investigated the creep-fatigue interaction of SLM AlSi10Mg alloy. Bao et al. (2021) recently used a macroscale large-scale testing machine to explore the hot dwell-fatigue properties of SLM AlSi10Mg alloy under strain control from room temperature to 400 °C and found that the fatigue behaviors were broadly the same for pure fatigue and dwell-fatigue. The creep-fatigue interaction associated with the microstructure thus needs to be further studied using an in-situ SEM.

Crystal plasticity modeling is an important micromechanics simulation method used to analyze the macroscopic deformation and failure of crystal materials. Computational crystal plasticity finite element (CPFE) modeling has been gradually developed since the 1980s and many researchers have worked on applying this method to many different materials. Asaro et al. used the critical resolved shear stress as the slip criterion and applied their crystal plasticity model in analyzing the elastic–plastic deformation behavior of face-centered cubic (FCC) materials (Asaro 1983). Anand et al. introduced a rate-dependent CPFE method to determine the active slip system in FCC materials (Anand and Kothari 1996). Han et al. developed a mechanism-based strain gradient plasticity model that incorporates the concept of geometrically necessary dislocation (GND) to achieve the hardening effect in their CPFE model by extending the Taylor hardening relation (Han et al. 2005). The length scale effect and GND density have been considered in a CPFE model to study local slip and the hardening effect of grain boundaries as well as the size effect (Dunne et al. 2007a). Computational CPFE modeling based on experimentally characterized microstructures can accurately predicted localized plastic deformation and provides access to full-field stress and strain distributions at the grain level (Dunne et al. 2007a). CPFE simulation combined with experimental high angular resolution electron backscattered diffraction (EBSD) and digital image correlation methods can capture the full-field stress, strain and GND distribution under different loading regimes (Dunne et al. 2007b). Experiments and CPFE simulations both showed that the GND density and plastic strain are distributed heterogeneously at the Ni matrix/hard particle interface (Dunne et al. 2012a, b, c). These methods were also used to study increases in the plastic strain, residual stress and GND density due to the thermal expansion mismatch between the matrix and inclusion in Ni superalloy (Zhang et al. 2014). The CPFE method has been used in predicting that triple junctions are the preferential crack initiation points in both the low-cycle fatigue and high-cycle fatigue of nickel superalloys (Manonukul and Dunne 2004). The method has also been used to verify energy dissipation criteria in the prediction of the fatigue crack initiation and fatigue life of FCC materials (Korsunsky et al. 2007). Similar CPFE fatigue crack studies have been conducted for HCP alloys (Zheng et al. 2016; Wilson et al. 2018). Besides the effect of plastic strain, the effect of elastic strain on fatigue crack nucleation had been studied, and an elastic stored energy criterion that 5% of the total work is stored as energy that affects fatigue crack nucleation had been used to accurately predict crack nucleation locations in nickel superalloys (Chen et al. 2018; Wan et al. 2014).

The present paper investigates the high-temperature dwell-fatigue behavior of SLM AlSi10Mg alloy and reports on a series of in-situ dwell-fatigue experiments with dwell times of 0, 60 and 120 s performed under the SEM at elevated temperature. The fracture evolution process of SLM AlSi10Mg alloy is observed and analyzed on the basis of the in-situ SEM images and ex-situ fracture morphology. The effect of the dwell time on the life cycle of materials is studied and a CPFE model is developed on the basis of the representative microstructure of SLM AlSi10Mg to reproduce the dwell-fatigue damage evolution. In addition, a high stress concentration around the notch that is strongly related to sample crack nucleation is simulated and discussed.

2 Experimental process and CPFE simulation

2.1 Sample preparation and characterization

An EOS M M290 machine, which was constructed by EOS GmbH in Germany, was used to print AlSi10Mg test pieces adopting the SLM system. The parameters

used in the manufacturing process are given in Table 1. The particle size of the raw material powder obtained from the EOS GmbH ranged 18–58 μm. Table 2 gives the chemical composition by weight percentage (*wt %*) of the AlSi10Mg alloy used in our experiments. To reduce the subsequent machining process of test pieces, test pieces were directly printed with a dog-bone shape and a U-shaped single edge notch located at the center of the gauge section. Geometric dimensions of the specimen are shown in Fig. 1. Three groups of specimens were produced with different laser scanning speeds.

The residual stress of the specimens, generated in the manufacturing process, was eliminated at 300 °C for 2 h before the test pieces were removed from the support structure (Maamoun et al. 2018). These fatigue specimens were then cooled to room temperature. Figure 2a shows the surface morphology of SLM AlSi10Mg alloy before polishing. The rough original surface made it impossible to clearly observe the crack propagation and microstructure evolution in real time. We therefore used SiC paper with grit scales of the 600, 1200, 3000 and 5000 W to polish the specimens. Finally, 0.5 μm SiO_2 milling liquid was used for vibration polishing. The final mirror-like surface is shown in Fig. 2b. Meanwhile, the three-dimensional (3D) internal structure of the SLM AlSi10Mg alloy was reconstructed using a micro-CT (Zeiss Metrotom, Germany) at an accelerating voltage of 225 kV, and the resolution adopted in the test process was 2 μm. The statistical results of equivalent pore diameters are shown in Fig. 2c. It is seen that the specimens obtained at a laser scanning speed of 1000 mm/s had the smallest pore distribution. Therefore, in our experiment, this group of specimens was used to study the dwell-fatigue performance. The typical 3D pore structure of SLM AlSi10Mg obtained at a laser scanning speed of 1000 mm/s is shown in Fig. 2d. It is seen that most of the pores are spherical.

2.2 In-situ SEM dwell-fatigue method

In-situ high-temperature dwell-fatigue experiments were carried out in the chamber of the SEM setup (SS-550, Shimazdzu, Japan), as shown in Fig. 3a. Stress control was adopted for the dwell-fatigue test, and the selected loading waveform was a trapezoidal wave, as shown in Fig. 3b. The creep effect was mainly reflected by the dwell time, T, in each cycle, which was the amount of time spent at maximum stress. When the dwell time T=0 s, the loading mode was referred to as pure fatigue. The maximum stress was σ_{max}=135 MPa, and the stress ratio was R=0.2. The stress rate was kept constant at 108 MPa/s during loading and unloading. The experimental temperature was set as 500 °C. According to the phase diagram of the Al-Si alloy, the phase transition temperature of AlSi10Mg alloy is about 577 °C (Haizhi et al. 2003). Therefore, the selection of 500 °C as the experimental temperature doesn't cause significant microstructure change. In the meantime, the significant creep effect of the SLM AlSi10Mg alloy at this temperature could appear within the experimental time allowed by the SEM in-situ experiment. Three group experiments were conducted with dwell times of 0, 60 and 120 s. Each group contained two specimens. For different numbers of cycles, the specimen surface near the notch was observed in the SEM to record the evolution of the surface microstructure. Finally, a high-resolution field-emission SEM (Quanta 450, FEI, America) was used to characterize the fractographic morphology of the failed specimens.

2.3 CPFE modeling methodology

The CPFE method has been developed over a few decades and applies in simulating the deformations of different alloy systems. It has been shown to accurately calculate the strain and stress response from a single crystal to multiple grains over a wide range of length scales (Dunne et al. 2007a; Zhang et al. 2014;

Table 1 SLM processing parameters of the AlSi10Mg alloy

Laser power P_L (W)	Laser spot diameter (mm)	Laser profile	Hatch distance Δy_s (mm)	Layer thickness D_s (mm)	Preheat temperature (°C)	Scanning speed v_s (mm/s)
370	0.20	Gaussian	0.08	0.03	220	700, 1000, 1300

Table 2 Chemical composition of the SLM AlSi10Mg alloy (wt %)

Element	Al	Cu	Fe	Mg	Mn	Si	Ti	Zn
Content	balance	0.04	0.07	0.29	0.06	6.30	0.01	0.10

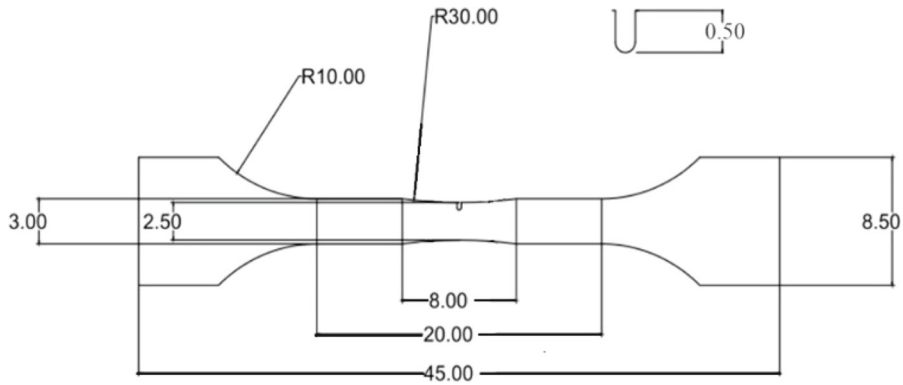

Fig. 1 Geometry of the fatigue test specimens (unit: mm)

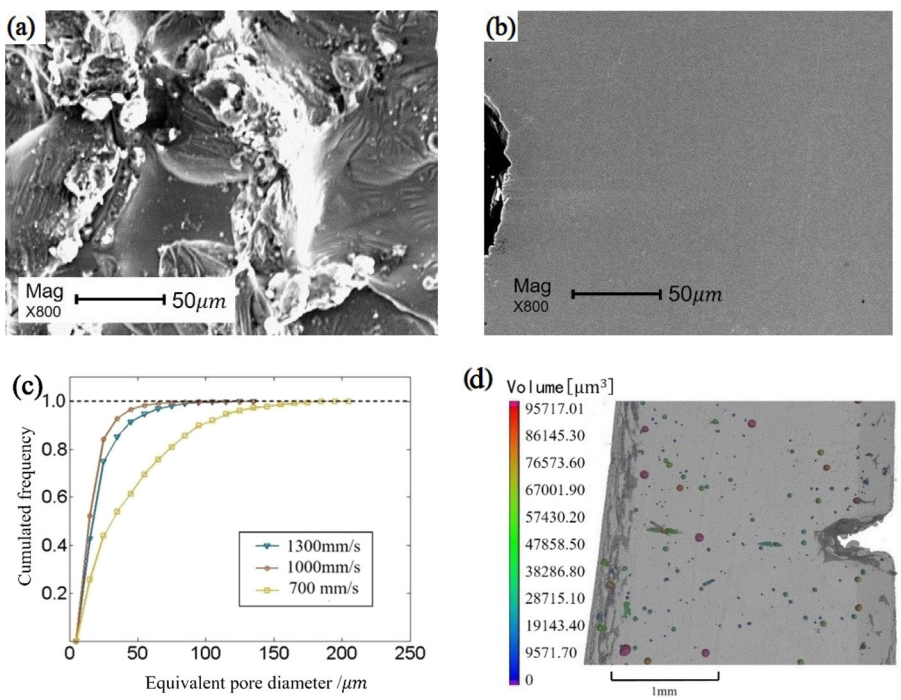

Fig. 2 **a** Surface of the unpolished AlSi10Mg specimen; **b** surface of the polished AlSi10Mg specimen; **c** relationship between the equivalent pore diameter and cumulated frequency; **d** typical 3D pore reconstruction from the micro-CT for SLM AlSi10Mg alloy fabricated at a laser scanning speed of 1000 mm/s

McGinty and McDowell 2006; Dunne et al. 2012a, b, c). Therefore, the CPFE is used to predict the deformation behavior and crack nucleation of SLM AlSi10Mg alloy under fatigue and dwell-fatigue. The crystal plasticity deformation is based on separating the total deformation gradient F into elastic and plastic parts (Lee 1969):

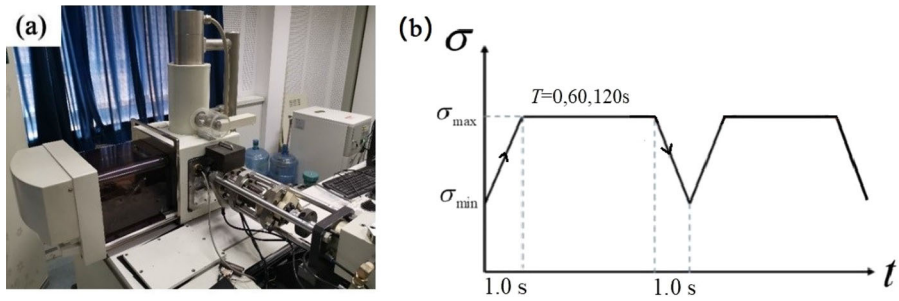

Fig. 3 Testing platform and loading profile: **a** Shimadzu in-situ SEM fatigue setup and **b** dwell-fatigue loading waveform

$$F = F^e F^p. \tag{1}$$

The elastic part F^e follows the generalized Hook's law, which contributes to rigid body rotation and lattice deformation. The plastic part F^p depends on the crystallographic slip movements with slip direction s and slip plane n. The total deformation rate D may be split into the elastic deformation rate D^e and plastic deformation rate D^p:

$$D = D^e + D^p. \tag{2}$$

D^e can be calculated using Hooke's law whereas D^p is determined by the slip rule for crystal plasticity. The slip rule used in this work was introduced by Dunne et al. (2007a), who considered the thermally activated escape of dislocations from obstacles. D^p is the symmetric part of the plasticity velocity gradient L^P, which is defined as

$$L^P = \dot{F}^p F^{p^{-1}} = \sum_{i=1}^{N_s} \left(\dot{\gamma}^i s^i \otimes n^i\right), \tag{3}$$

where $\dot{\gamma}^i$ is the shear strain rate of a specific slip system and $\boldsymbol{n}^i$ and $\boldsymbol{s}^i$ are respectively the slip plane normal and slip direction vector of the slip system. The shear strain rate $\dot{\gamma}^i$ is calculated as

$$\dot{\gamma}^i = \rho_m v_g b, \tag{4}$$

where ρ_m is the mobile dislocation density, v_g is the average dislocation glide velocity, and b is the magnitude of Burger's vector (Cottrell 1953). Gibbs argued that local thermal activation events are needed to free the pinned dislocations for glide to occur (Gibbs 1969). The average glide velocity is defined by

$$v_g = \frac{dvb}{2l} \exp\left(-\frac{\Delta G}{kT}\right), \tag{5}$$

where v is the frequency of dislocation attempts to jump the energy barrier, k the Boltzman constant, T the temperature, ΔG the Gibbs free energy,l the pinning distance of a dislocation and d the length of a thermal activation event (Granato et al. 1964). Considering the work carried by the stress field, the Gibbs free energy is

$$\Delta G = \Delta F - \tau \Delta V, \tag{6}$$

where ΔF is the Helmholtz free energy and $\Delta V = lb^2$ is the activation volume. The effective stress field that drives the thermal activation event is $\tau^* = \tau - \tau_c$, where τ is the resolved shear stress and τ_c is the corresponding critical resolved shear stress (Taylor 1934). The work done by the effective stress field is $\tau^* \Delta V$ and the slip rate of the i th slip system is then

$$\dot{\gamma}^i = \rho_m b^2 v \exp\left(-\frac{\Delta F}{kT}\right) \sinh\left[\frac{\Delta V}{kT}\left(\tau^i - \tau_c^i\right)\right], \tag{7}$$

where the Helmholtz free energy ΔF is the activation energy for the dislocation escape from obstacle pinning and ΔV is the activation volume. The velocity gradient is then given as

$$L^P = \sum_{i=1}^{N_s} \rho_m b^2 v \exp\left(-\frac{\Delta F}{kT}\right) \sinh\left[\frac{\Delta V}{kT}\left(\tau^i - \tau_c^i\right)\right] s^i \otimes n^i, \tag{8}$$

On the basis of Taylor's dislocation hardening model, dislocations provide shear resistance and the critical resolved shear stress τ_c increases with the dislocation density. The hardening rule is expressed as

$$\tau_c = \tau_{c0} + G_{12} b \alpha \sqrt{\rho_{SSD} + \rho_{GND}}, \quad (9)$$

where τ_{c0} is the initial critical resolved shear stress, G_{12} is the shear modulus and α is the dislocation interaction coefficient, which is simply taken to be unity in the absence of other knowledge. The dislocation density is divided into the density of statistically stored (ρ_{SSD}) and geometrically necessary (ρ_{GND}) dislocations. The evolution of the SSD density relates to the accumulated plastic strain rate $\dot{p}$ as expressed by

$$\rho_{SSD} = \lambda \dot{p}, \quad (10)$$

where λ is the accumulation rate determined from experimental hardening observations, and the hardening is isotropic. In a slip plane, the direction s of the screw dislocation line segments and the directions n (the plane normal) and m ($= s \times n$) of the edge dislocation line segments are included in the calculation of the geometrically necessary dislocation density (Dunne et al. 2007a). The GND density distribution is obtained from strain gradients accommodating lattice curvature (Busso et al. 2000). Nye's dislocation tensor Λ is used to calculate the GND density according to

$$\Lambda = curl(F^p) = \sum_{i=1}^{N} \left(\rho_s^i b^i \otimes s^i + \rho_{em}^i b^i \otimes m^i + \rho_{en}^i b^i \otimes n^i \right), \quad (11)$$

where ρ_s^i is the screw component of slip system i, and ρ_{em}^i and ρ_{en}^i are the edge components of the corresponding slip system. However, for crystals with high degrees of symmetry, Eq. (11) has infinite solutions of GND components and the GND density can be obtained only by introducing constraints (Dunne et al. 2012a, b, c). Two constraints are developed for solving the non-uniqueness problem: the L_1-norm for the minimization of stored energy and the L_2-norm for the minimization of the dislocation line length (Arsenlis and Parks 1999; Kysar et al. 2010). The constraints are expressed as

$$L_1 = \sum_{i=1}^{N} \left| \rho^i \omega^i \right| \; and \; L_2 = \left[\sum_{i=1}^{N} \left(\rho^i \omega^i \right)^2 \right]^{1/2}, \quad (12)$$

where ω denotes possible weightings. In this study, the L_2-norm minimization was used to calculate the GND density of different hard-facing alloys. The squares of edge and screw dislocation density components in each slip system are summed in calculating the GND density minimal:

$$\rho_{GND} = \sqrt{\sum \left(\rho_s^i\right)^2 + \left(\rho_{em}^i\right)^2 + \left(\rho_{en}^i\right)^2}. \quad (13)$$

2.4 Calibration of material properties

Calibrations were initially carried out on a polycrystal AlSi10Mg sample to obtain correct average stress–strain responses. An EBSD-captured grain map for one representative sample is shown in Fig. 4a. AlSi10Mg alloy has a homogeneous distribution of the grain size with an average size of 10 μm. The crystal orientations of 125 grains were extracted from the EBSD result as representative crystal orientations. Correspondingly, the 50 μm × 50 μm × 50 μm cubic calibration model with 125 cubic grains shown in Fig. 4b was created to simulate the tensile deformation of AlSi10Mg under a strain rate of $1 \times 10^{-3} s^{-1}$ for calibration of the CPFE slip role parameters. The bottom surface of the model was fixed in the y-direction and a uniaxial y-direction tensile displacement load was applied to the top surface to obtain the stress–strain properties. An element size of 1 μm was used to ensure both accuracy and speed of the calibration. Representative crystal orientations were extracted from the EBSD results and assigned to the calibration model.

Notched dog-bone AlSi10Mg samples were used in fatigue and dwell-fatigue tests. The samples commonly fractured at the notch owing to the heterogeneity of the notch-induced stress. The region of interest (ROI) of the sample was thus selected as the region below the notch edge and a corresponding CPFE model was built as shown in Fig. 4c. The EBSD technique only provides information of the two-dimensional microstructure crystal orientation and the microstructure varies among different samples. To simplify the simulation process and maintain the uniformity of the microstructure for comparing the effects of different loading modes, the CPFE model of the ROI was set in a quasi-3D manner with dimensions of 400 μm × 400 μm × 10 μm by extruding artificially created hexagonal grain morphologies in the z-direction to obtain a "bamboo" structure. The model contained more than 100 hexagonal grains with size of 10 μm and was meshed with 1 μm

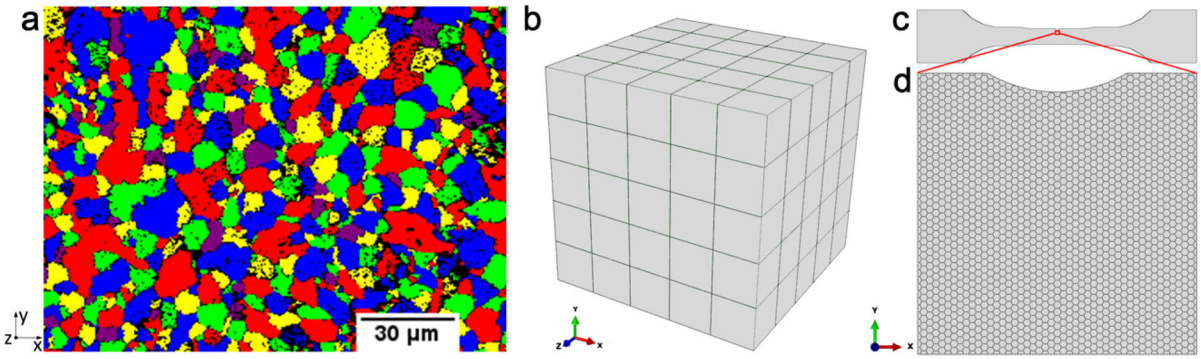

Fig. 4 EBSD data and corresponding CPFE models: **a** grain map of a region of interest in an AlSi10Mg sample; **b** CPFE tensile test model containing 125 cubic grains for parameter calibration; **c** continuum finite element model for acquiring the boundary condition of the ROI; **d** CPFE model of the ROI with dimensions of 400 μm × 400 μm × 10 μm and 1863 hexagonal grains

C3D20 elements in a finite element calculation. The same element size was used in building all models to obtain accurate strain and GND density distributions. Although the quasi-3D model was not fully representative of the subsurface microstructure, it had successfully reproduced the deformation process in many other cases (Dunne et al. 2007b; Dunne et al. 2012a, b, c). Although far fewer than the thousands of loading cycles in reality, 10 cycles of fatigue or dwell-fatigue loading were applied to models to evaluate the effects of the different loading methods on the deformation and failure of the samples. The geometry, microstructure, crystal orientations and boundary conditions were kept the same for each CPFE model to eliminate their effects. As shown in Fig. 4d, a continuum finite element model was built on the basis of the shape and mechanical properties of the test samples. A force was applied to the dog-bone ends to provide an average x-direction stress of 135 MPa, and the stress distribution around the ROI was then recorded as accurate boundary conditions for subsequent simulations.

Crystal orientations in the CPFE model were carefully selected from the EBSD experiment results. Pole figures obtained using the EBSD technique and the calibration model are presented in Figs. 5a and b. The AlSi10Mg sample showed strong texture around [101], and these orientations were assigned to both calibration and fatigue-test CPFE models.

Stress–strain curves obtained by experiment and simulation are shown in Fig. 6. The AlSi10Mg sample yields at 150 MPa at 500 °C and shows good ductility but low work hardening capacity. The

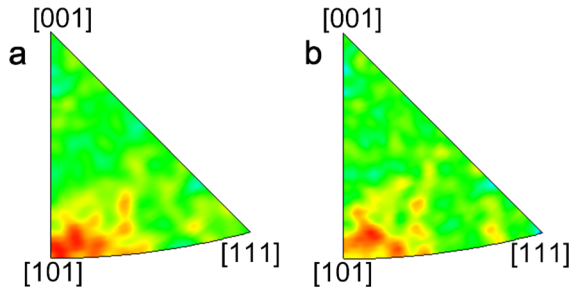

Fig. 5 Crystal orientation distribution in an AlSi10Mg sample and from the experiment and the CPFE model of the ROI: **a** inverse pole figure captured using the EBSD technique and **b** inverse pole figure derived from the polycrystal CPFE model

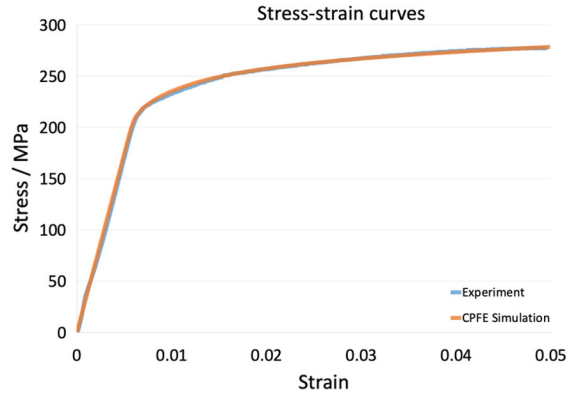

Fig. 6 Stress–strain curves of SLM AlSi10Mg alloy at 500 °C obtained by experiment and CPFE modeling

simulated stress–strain curve obtained from the CPFE calibration model matched the experimental result, which ensured an accurate elastic–plastic response in subsequent fatigue simulation. Calibration was

carried out at 500 °C. The calibrated crystal plasticity slip rule parameters are listed in Table 3.

The Helmholtz free energy ΔF of $2.6 \times 10^{-20} J/\text{atom}$ is the activation energy for dislocations to escape obstacle pinning. The activation volume in AlSi10Mg depends on the Burgers vectors, the length of the activation event l and the overall obstacle density. Because l is approximately equal to the magnitude of the Burgers vector $\boldsymbol{b}$ and the spacing of obstacles is 0.1 μm, the activation volume ΔV is $1.66 \times 10^{-6} \mu m^3$.

3 Results

3.1 Experimental results

3.1.1 Fatigue life at different dwell times

First, the cycle lifetimes of fatigue test pieces having different dwell times are shown in Fig. 7a, where the lifetime is expressed as the number of loading cycles until final fracture. In Fig. 7a, the y-axis adopts a logarithmic coordinate. It is seen that the lifetime is much longer for pure fatigue than for dwell-fatigue, with the average lifetime of specimens having a dwell time of 60 s being 94.40% shorter. The lifetime decreases for a longer dwell time. This trend is consistent with the lifetime trend of most metal materials, such as nickel-based superalloys (Chen et al. 2013; Hu et al. 2016) and Ti-6Al-4 V alloys (Everaerts et al. 2017). This is mainly because the service life of materials is controlled by the damage in each loading cycle. Under dwell-fatigue, the total damage in a loading cycle comprises fatigue damage, creep damage and damage due to their interaction. The creep damage of dwell-fatigue is mainly due to the repeated effect of primary creep deformations. Therefore, with an increase in the dwell time in each loading cycle, the primary creep deformation gradually increases, which aggravates the creep damage and total damage to the SLM AlSi10Mg alloy (ZrÍnk et al. 2001). Therefore, the result is that the lifetime decreases gradually with a lengthening of the dwell time.

Inelastic strain can be used to characterize the degree of damage to materials. Figure 7b presents the relationship between the accumulating inelastic strain and number of loading cycles. Refer to the author's previous work (Wang et al. 2020) for the method of calculating the accumulated inelastic strain for dwell-fatigue. Figure 7b shows the accumulated inelastic strain in the first 250 cycles because the lifetime is much longer for pure fatigue than for dwell-fatigue. It is seen that the inelastic strain accumulated under dwell-fatigue is greater than that accumulated under pure fatigue. Additionally, the accumulated inelastic strain increases almost linearly with the number of loading cycles. However, when the dwell time is introduced to the peak stress of each cycle, the accumulated inelastic strain no longer has a linear relationship with the number of loading cycles. This

Table 3 Calibrated slip rule parameters

Slip rule parameter	Value	Unit
Dislocations jump frequency f	1×10^{11}	s^{-1}
Burgers vector $\boldsymbol{b}$	4.08	Å
Boltzmann constant k	1.381×10^{-23}	-
Helmholtz free energy ΔF	2.6×10^{-20}	J/atom
Poisson's ratio v	0.3	-
Initial mobile dislocations density ρ_{ssdm}	0.01	μm^{-2}
Overall obstacle density ρ_0	0.01	μm^{-2}
Activation volume ΔV	8.18×10^{-7}	μm^3
Critical resolved shear stress τ_c	70	MPa
Hardening coefficient γ_{st}	10	μm^{-2}
Young's modulus E	20	GPa
Shear modulus G	7.7	GPa

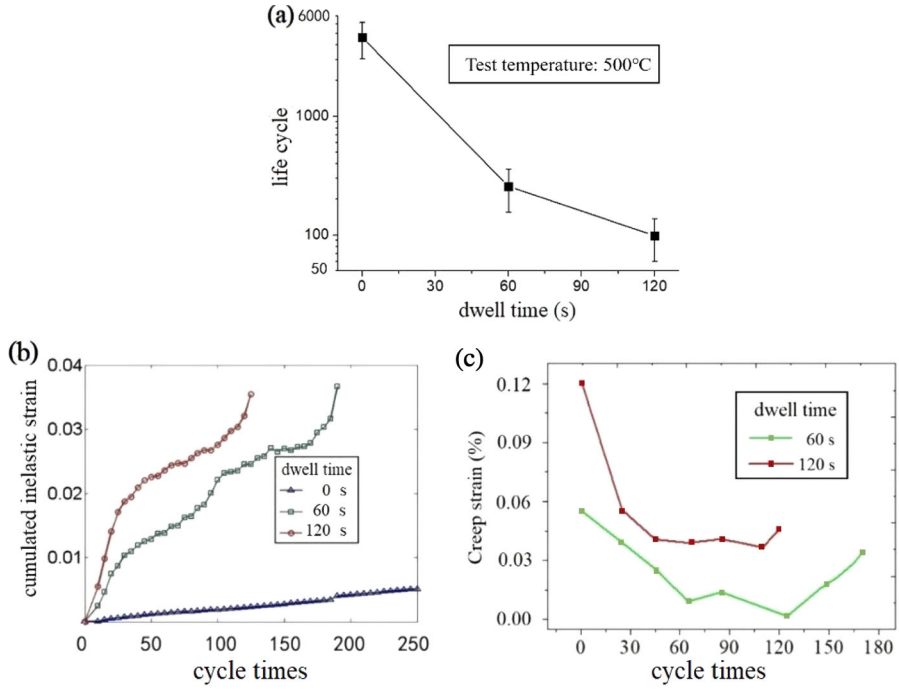

Fig. 7 **a** Relationship between the lifetime measured in loading cycles and dwell time; **b** relationship between the accumulating inelastic strain and the number of loading cycles for different dwell times; and **c** the relationship between the creep strain and the number of loading cycles for different dwell times

is mainly because additional plastic strain is introduced during the dwell periods. Usually, the creep curve remains nonlinear throughout the lifetime of SLM AlSi10Mg alloy in a high-temperature creep environment (Uzan et al. 2018).

To better explain the adverse effects of the dwell time on the lifetime, the creep strain generated during the dwell periods is calculated for each loading cycle, as shown in Fig. 7c. Creep strain is higher for a dwell time of 120 s than for a dwell time of 60 s. In addition, with an increasing number of loading cycles, the creep strain follows a trend of first decreasing, then stabilizing and finally increasing. The trend is similar to that of pure creep deformation (Uzan et al. 2018), which indicates that creep damage plays an important role in the dwell-fatigue process of SLM AlSi10Mg alloy. The increase in inelastic strain in the third creep stage mainly relates to the damage evolution of the alloy, the generation and aggregation of voids and formation of microcracks.

3.1.2 Process of crack growth for different dwell times

In this section, we observe the crack initiation and propagation process of AlSi10Mg alloy under pure fatigue and 120 s of dwell-fatigue at a high temperature of 500 °C in real time. Figure 8 presents the surface evolution morphology of a fatigue test piece near the notch in different fatigue cycles. A hemispherical surface pore 1, located in an upper left position as shown in Fig. 8a, is filled with AlSi10Mg powder because the AlSi10Mg powder has not completely melted. As shown in Figs. 8b, c, cracks 1 and 2 initiate at the notch position of the specimen in the 2100th and 5287th cycles, respectively. Additionally, pore 1 gradually separates from the filling powder and then forms visible microcracks. Furthermore, subsurface pores near pore 1 gradually crack, as seen in Fig. 8c–e. For crack 1 near the notch, there is no obvious propagation along the initial direction from the 2100th cycle to the 5287th cycle, which mainly relates to the square particles above it. From the 5287th cycle to the 5661th cycle, there is large plastic deformation at the tip of crack 1, as shown in Fig. 8e. Figure 8f shows the near-notch morphology of the specimen before instantaneous fracture. The final fracture of the crack is from the upper edge of the square particles and propagates in a direction perpendicular to the loading direction. At the same time, because the mechanical properties of the molten pool boundary during the SLM

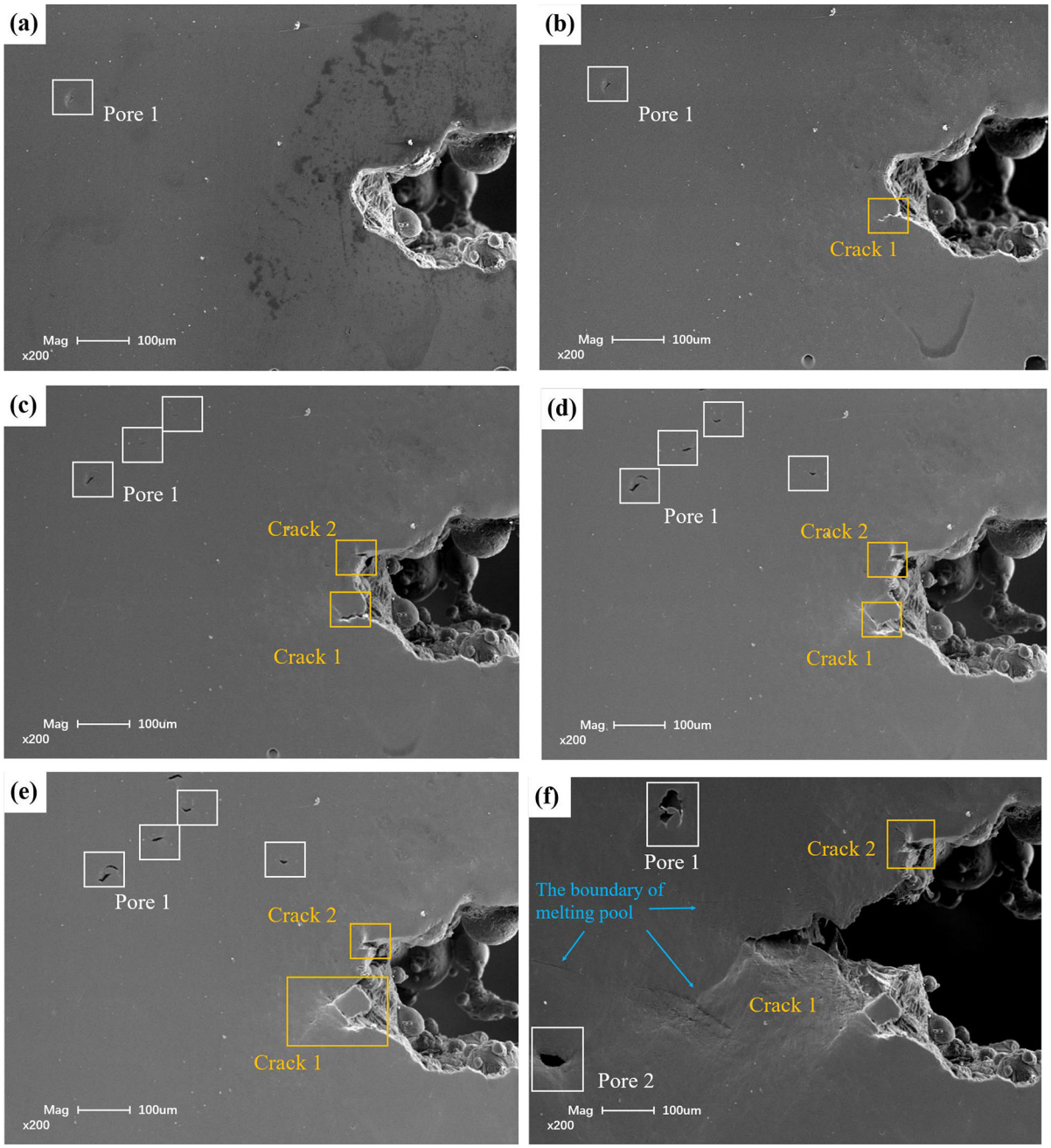

Fig. 8 In-situ fatigue crack growth at 500 °C: **a** 0th cycle; **b** 2100th cycle; **c** 5287th cycle; **d** 5585th cycle; **e** 5661st cycle; and **f** 5726th cycle

manufacturing process are different from those at other positions (Li et al. 2021), arc lines appear where there is large plastic deformation, as shown in Fig. 8f. In addition, subsurface pores gradually grow owing to large plastic deformation and form fish-eye-like cracks, as shown by Pore 2 in Fig. 8f.

Figure 9 shows evolutionary morphology images of the surface for the SLM AlSi10Mg alloy specimen when the load is maintained for 120 s at peak stress. Similar to what is observed in Fig. 8a, there is a hemispherical pore filled with unmelted powder on the surface of the test piece in Fig. 9a. Near the edge

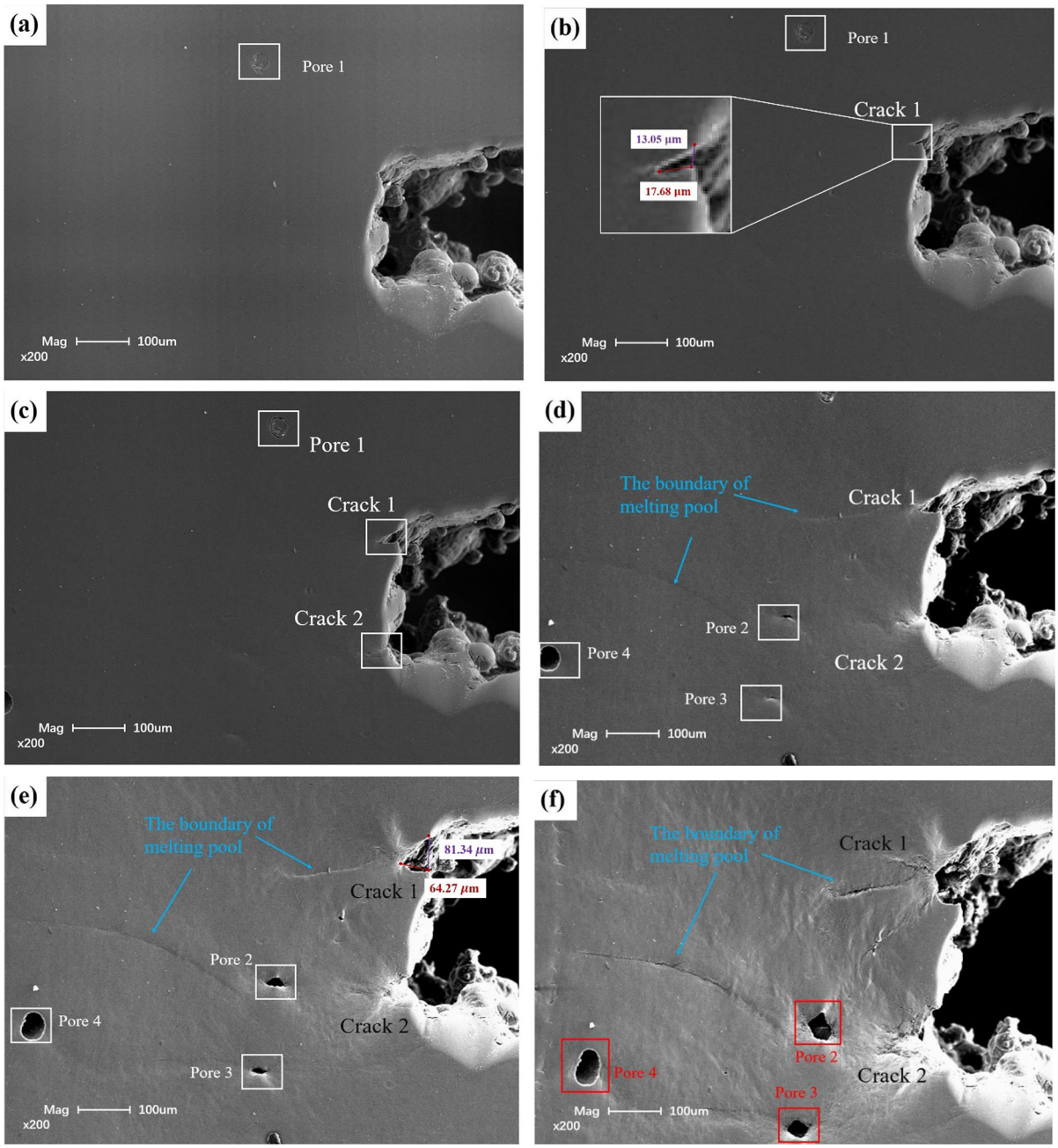

Fig. 9 In-situ crack growth for fatigue with a dwell time of 120 s at 500 °C: **a** 0th cycle; **b** 45th cycle; **c** 87th cycle; **d** 102th cycle; **e** 117th cycle; and **f** 124th cycle

of the notch, crack 1 initiated in the 45th cycle, as shown in Fig. 9b. From the 45th to 117th cycle, the length of crack 1 grew from 17.68 to 64.27 μm. However, the opening displacement of the crack mouth increased from 13.05 to 81.34 μm. At the lower edge of the notch, crack 2 began sprouting from the 87th cycle. However, crack 2 did not propagate appreciably from the 87th to 124th cycle, and there was only plastic deformation near the crack tip. In addition, arc lines formed on the surface of the test piece, as shown in Figs. 9d–f. Meanwhile, the hemispherical surface pores became long, parallel to

the loading axis, while the subsurface pores firstly formed microcracks and then became fish-eye-shaped cracks, but the cracks did not continuously propagate at the two ends. Along the loading axis, the opening distance of the fisheye was larger, which indicated that the deformation of subsurface pores was more severe under dwell-fatigue.

By comparing the crack growth process under pure fatigue and dwell-fatigue of 120 s, although cracking initiated near the notch under both load conditions, the propagation length was much longer under pure fatigue than under dwell-fatigue, which mainly relates to the stress state at the crack tip. When the specimen was subjected to peak stress during the dwell time of 120 s, there was a larger region of plastic deformation near the crack tip at 500 °C, resulting in blunting of the crack tip. Compared with the case of pure fatigue, the stress concentration at the crack tip is greatly reduced (Suresh 1998). The stress intensity factor at the crack tip also decreases. As a result, the rate of crack growth decreases and even falls to zero. There is instantaneous tearing when the plastic deformation of the test pieces approaches the fracture strain of the SLM AlSi10Mg at 500 °C.

3.1.3 Fractography analysis

Analysis of the cycle life in Sect. 3.1.1 revealed that the introduction of a dwell time reduces the lifetime, which mainly relates to creep damage during the dwell time. The fracture morphology and high-resolution microstructure image of the failed specimen are presented in Fig. 10. At 500 °C, there were many dimples and deep pores in the fracture surface, as shown in Figs. 10a–c, which indicates that the fracture characteristic of the SLM AlSi10Mg alloy is ductile fracture. A comparison of Figs. 10a–c clearly shows that the deep pores on the fracture surface are larger and deeper for dwell-fatigue of 120 s. A similar fracture surface was observed previously for SLM AlSi10Mg alloy under creep (Uzan et al. 2018). The fracture surfaces are further enlarged in Figs. 10d–f. For pure fatigue, several voids are seen at the Al/Si interface, but they are very small in Fig. 10d. However, for the specimen having a dwell time of 60 s, the number of creep voids is much higher. Not only does the number of creep voids increase appreciably but also the creep voids enlarge for dwell-fatigue of 120 s in Fig. 10f. In general, a creep pore is a typical characteristic of creep damage (Ding et al. 2018). A longer dwell time results in an appreciable increase in the proportion of creep damage in the total damage. As a result, the lifetime of the material is gradually reduced.

3.2 CPFE simulation results

A force equivalent to that in the experiment setup is applied to the continuum dog-bone shape crystal plasticity model and the stress distribution is calculated. The stress around the ROI is extracted as a boundary condition of the CPFE fatigue and dwell-fatigue models to simulate actual tension states.

The stress distribution map in Fig. 11 shows that at peak applied stress (135 MPa), a strong stress concentration around the notch forms a butterfly-shaped region of high stress. The boundary of the ROI bears both tensile and shear stresses. The accurate stress values are used in the following CPFE fatigue simulations. Results obtained using the pure-fatigue model are used to present CPFE simulation features.

The AlSi10Mg CPFE fatigue model is assigned with the calibrated slip rule parameters and the plastic strain distributions are shown in Fig. 12a. After 10 cycles of loading, the CPFE fatigue model forms several characteristic high-plastic-strain bands, which is consistent with the results for the other two dwell-fatigue models. These high-strain bands are oriented approximately 45° to the loading direction and have maximum values in grains near the notch. Differences among the assigned crystal orientations result in different resolved shear stress in each grain, which creates a heterogeneous plastic strain distribution in the polycrystal CPFE model.

A closer look at the plastic strain map in Fig. 12b reveals that the simulated high strains occur in some grains near the central notch edge, and intense persistent slip bands form from similar locations. Plastic strains in some grains near the notch exceed 10% while some grains are hardly plastically deformed. The crystal orientations of ‘hard’ grains result in the resolved shear stresses in these grains not reaching or only just reaching the critical resolved shear stress.

Figure 13 shows that the maximum plastic strain within the AlSi10Mg model increases by 3% in

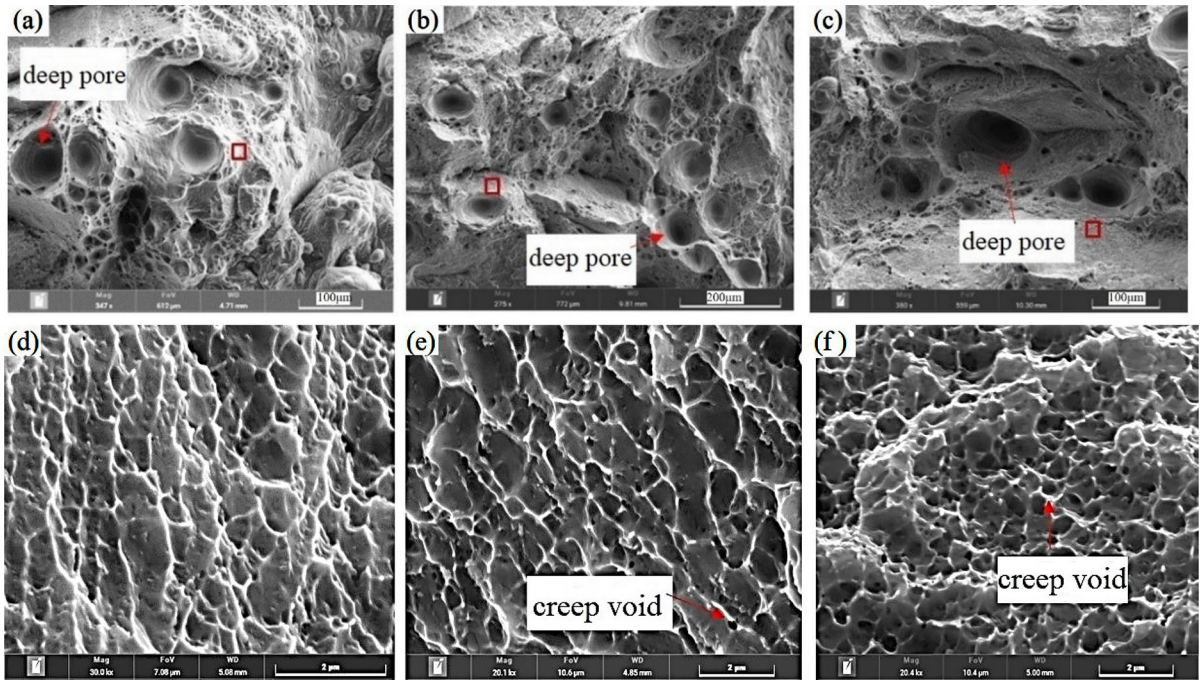

Fig. 10 Fracture surface for dwell times of **a** 0 s, **b** 60 s and **c** 90 s. High-resolution microstructure images for dwell times of **a** 0 s, **b** 60 s and **c** 90 s

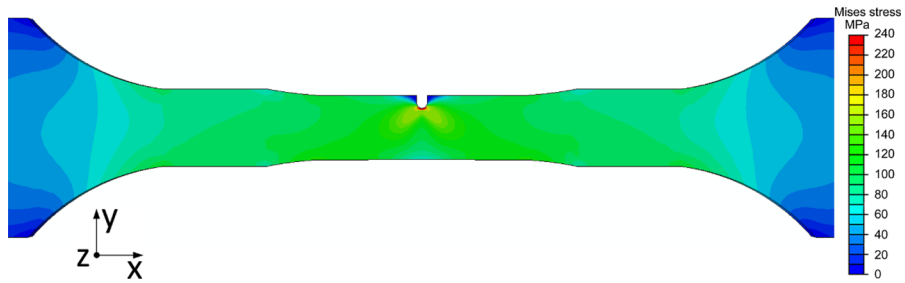

Fig. 11 Distribution of the Mises stress simulated using the continuum finite element model under a tensile load of 135 MPa

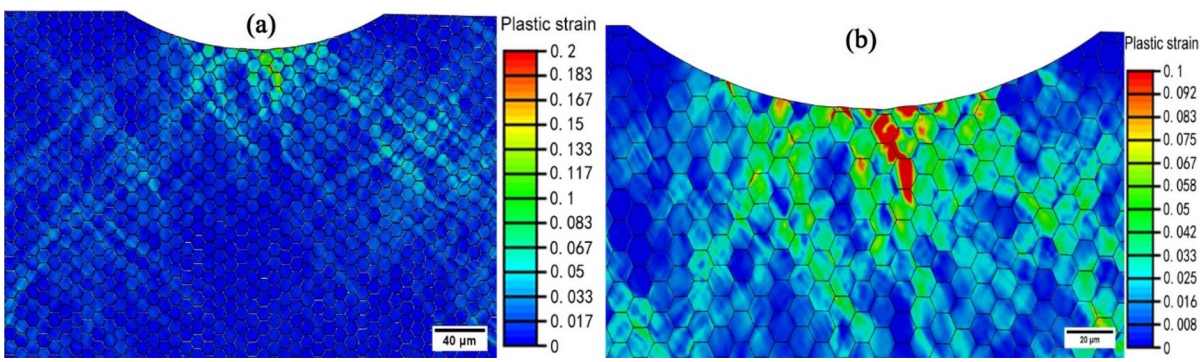

Fig. 12 **a** Plastic strain distribution; **b** Magnified plastic strain distribution in the AlSi10Mg CPFE model in the 10th cycle

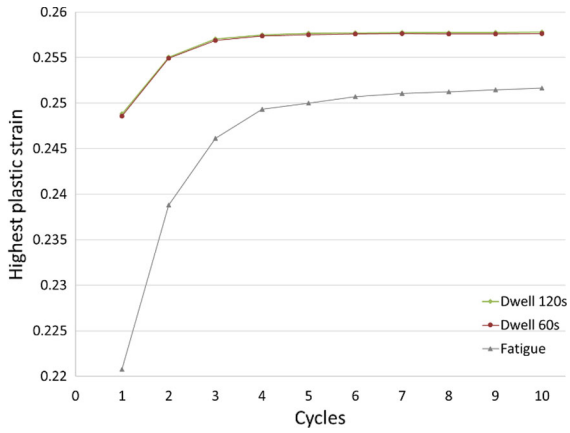

Fig. 13 Maximum plastic strain in AlSi10Mg CPFE models

fatigue simulation. The initial four cycles contribute most to the plastic strain increase, and the growth rate becomes steady after the fifth cycle for both fatigue and dwell-fatigue loading modes. The maximum plastic strain increases dramatically when the dwell time is introduced from the first cycle. However, the maximum strain seems insensitive to the dwell time in that the maximum strain for a dwell time of 120 s is only less than 1% higher than that for a dwell time of 60 s.

The plastic strain is a maximum on the right side of the front surface for pure fatigue as shown in Fig. 14a whereas the plastic strain is a maximum at the notch edge of the back surface for dwell-fatigue as shown in Fig. 14b. Considering different plastic strain levels for the two loading modes, as the number of loading cycle increases and more plastic strain accumulates, the sample may form several

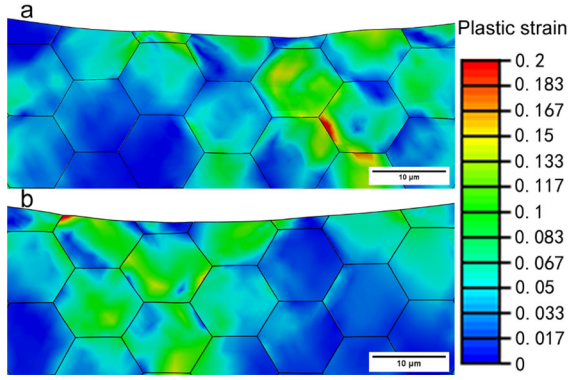

Fig. 14 Simulated plastic strain distribution in the ROI near the notch after 10 cycles: **a** front surface and **b** back surface

microcracks at different locations as seen in the experimental results in Figs. 8 and 9.

GND density maps derived from the CPFE model are presented in Fig. 15a. High values of the GND density are mainly distributed at the boundaries of severely plastically deformed grains in the near-notch region. Additionally, high GND densities are found at boundaries between severely and slightly deformed grains. The high plastic strain concentration in these "soft" grains potentially causes crack nucleation in these grains. The accumulation of high GND density at the soft–hard grain boundary increases the probability of microcrack formation at these positions (Jiang et al. 2016). Figure 15b shows that the stress in the CPFE model is distributed heterogeneously and high stress remains near the notch center. Stress in less-deformed grains is much higher than that in the severely deformed grains. The high stress concentration at the hard-soft grain boundaries makes these locations a hot spot for microcrack nucleation. The map of elastic stored energy in Fig. 15c shows that similar to the plastic strain map, there are high values of stored energy in these grains with high plastic strain and some grains with low plastic strain. This phenomenon indicates that some plastic deformation-free locations are hot spots for elastic energy storage and that microcracks probably nucleate at these locations as the number of loading cycles increases. The same process of microcrack formation is seen in Figs. 8 and 9.

4 Discussion

4.1 Failure mechanism

The fracture strain of SLM AlSi10Mg alloy increases gradually with an increase in temperature and even exceeds 55% at 400 °C (Uzan et al. 2018). This result supports that SLM AlSi10Mg alloy has high fracture toughness in a high-temperature environment. Additionally, in the case of our dwell-fatigue experiment, Fig. 9f shows that the area near the notch underwent large deformation before specimen failure. Therefore, the pores generated in the manufacturing process are elongated along the deformation direction. The fracture path of the specimen is along the short axis of the ellipsoidal pores, as shown in Fig. 16a, which is consistent with the results of other studies (Bao

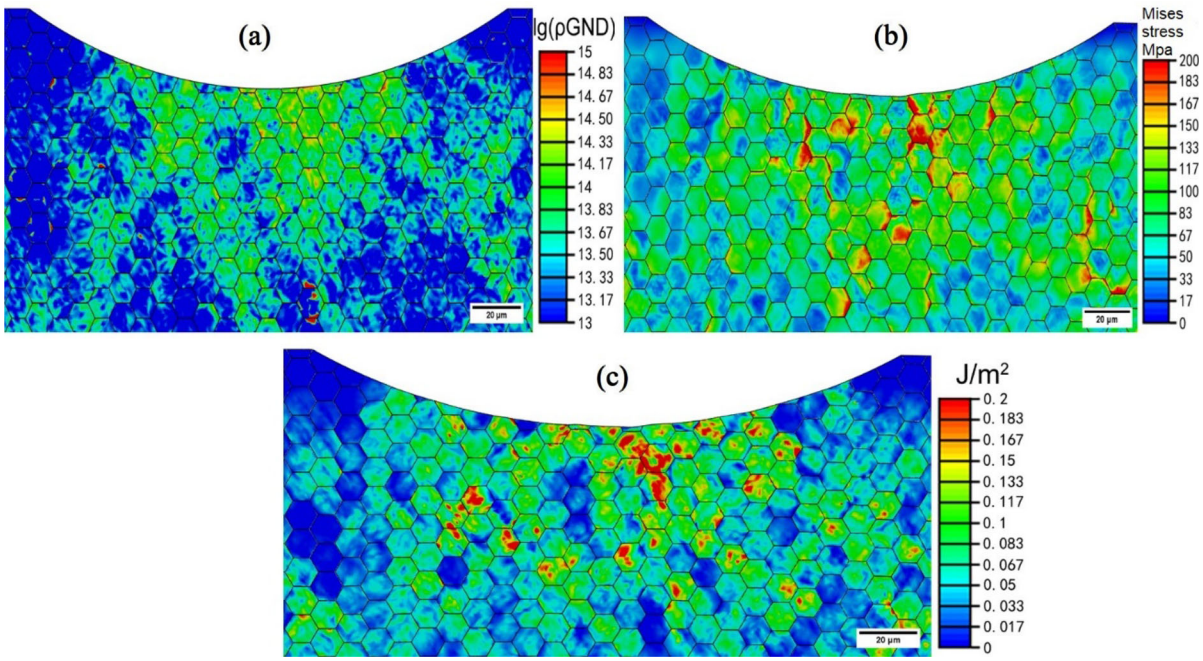

Fig. 15 **a** GND density distribution; **b** Mises stress distribution; and **c** stored energy distribution in AlSi10Mg alloy models in the 10th cycle

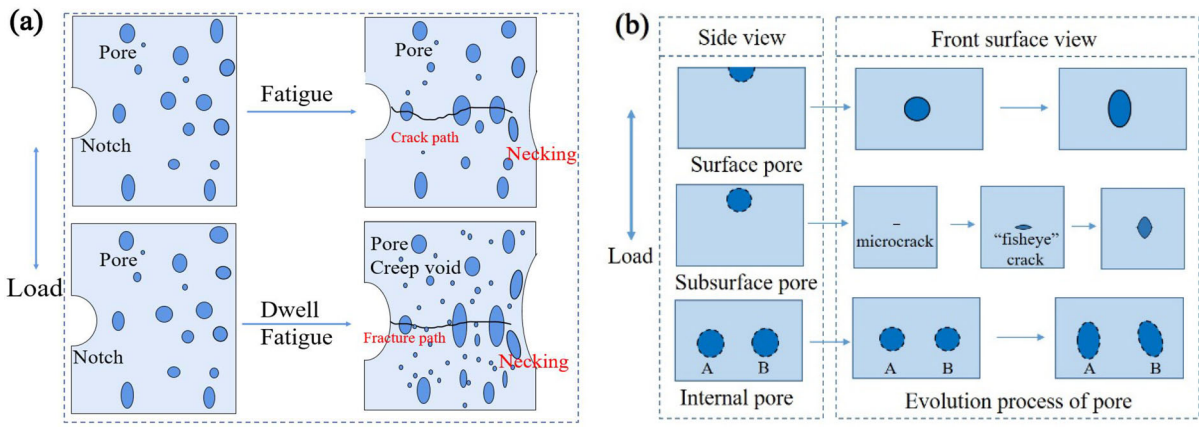

Fig. 16 Illustration of **a** the fracture path and **b** the evolution mechanism for pores at different positions

et al. 2020). When the dwell times are introduced, creep damage contributes to the overall damage of materials. According to the position of our experimental conditions on the Ashby deformation map for metallic alloys, the deformation mechanism is related to dislocation creep that is controlled by bulk diffusion under the condition of dwell-fatigue at 500 °C for SLM AlSi10Mg alloy (Kundu 2012). Therefore, a large number of creep micro-voids are generated and grow in the alloy for dwell-fatigue. Creep micro-voids and ellipsoidal pores gradually evolve and coalesce. This eventually leads to the instantaneous fracture of the material when the stress exceeds the fracture strength.

Pores are inevitable defects in SLM manufacturing. It can be seen from Fig. 2d that the distribution of pores is very random, including location, size, shape, etc. Therefore, the porosity is used as a parameter to evaluate the mechanical properties of materials. In generally, the higher the porosity, the lower the

fatigue life of the material (Wang et al, 2019). Besides, the observations presented in Sect. 3.1.2 show that the evolution of pores is inconsistent at different positions of specimens. Figure 16b shows the evolution mechanism of hemispherical surface pores, subsurface pores, and internal pores during dwell-fatigue. In-situ observations and fracture analysis reveal that the hemispherical pore and internal pore usually firstly undergo plastic deformation and gradually evolve from a spherical shape to an ellipsoid shape, and the long axis of the ellipsoid usually coincides with the direction of the loading axis (Bao et al. 2020). Under the synergistic effect of normal and shear stress (Kanvinde and Deierlein 2007), some ellipsoidal pores, which are located in the necking region, begin to incline. However, for the subsurface pores, the side close to the specimen surface fractures and forms microcracks and finally forms a large fish-eye crack, as shown in Fig. 16b. The stress concentration effect is more obvious because the two ends of the fish-eye crack are sharper. Therefore, the damage due to pore 2 is greater than that due to pore 1 and that due to pore 4 in Fig. 9f. In short, the subsurface pores cause more damage than the other two types of pores.

4.2 Plasticity-induced crack nucleation

The polycrystal CPFE model is used to simulate the high-temperature fatigue and dwell-fatigue behavior of a 10 μm thick layer of an AlSi10Mg sample having more than 100 grains. Because actual test samples are different from each other and EBSD characterization is not applied for each sample, a representative homogeneous 10-μm hexagonal grain microstructure is used for different loading modes. In contrast with the actual sample having internal pores, the CPFE model does not have porosity. Thus, the effect of pores is not explored in this part of the work. High-temperature pure fatigue and dwell-fatigue loading modes are compared. The effects of the crystal-orientation-induced stress, plastic strain and elastic stored energy on crack nucleation are presented and compared with experimental results for this polycrystal CPFE simulation.

Figure 17 compares the maximum GND density and stored elastic energy values after 10 loading cycles. Both the maximum GND density and stored energy increased quickly when the dwell time is

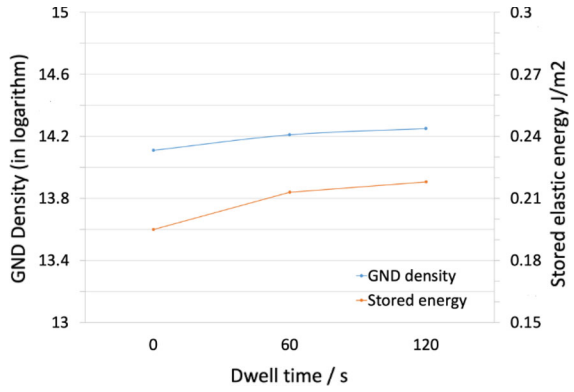

Fig. 17 The CPFE simulated GND density and stored elastic energy of each sample after 10 loading cycles

firstly introduced but the growth rate drops as the dwell time continually increases. Therefore, for dwell-fatigue, the maximum GND density and stored energy do not change linearly with the dwell time. High local plastic strain has a strong relationship with crack nucleation, and the maximum plastic strain accumulating around the notch directly causes microcrack nucleation at these locations. The high stress concentration at soft-hard grain boundaries raises the possibility of brittle fracture at these locations. Figures 12b, 15b, c show that there is high plastic strain in some grains located in the stress-concentration region, but there are also locations of high stored energy in some less plastically deformed grains. The local stress at these locations is not high enough to cause massive plastic deformation, but the continuous low stress results in damage in these areas. The stored elastic energy criterion explains why some microcracks nucleate far from the most plastically deformed area as commonly found in the experiment results. The dwell period directly increases the maximum plastic strain, which results in the shorter lifetimes of these dwell-fatigue samples. However, increasing the dwell time does not have a linear effect on the maximum plastic strain.

5 Conclusion

We conducted fatigue and dwell-fatigue tests on SLM AlSi10Mg at 500 °C. The mechanical response, damage evolution and fracture mechanism were systematically analyzed and the effect of the dwell time on the fatigue fracture behavior was studied.

Additionally, through CPFE simulation, the crack nucleation and evolution mechanism of the material near the notch was studied. The following findings are taken from the experimental and simulation results.

(1) For the SLM AlSi10Mg alloy, the dwell-fatigue lifetime is much shorter than that of the fatigue at 500 °C, with the average lifetime of specimens having a dwell time of 60 s being 94.40% lower. At 500 °C, creep damage plays a dominant role in creep-fatigue interaction loading.
(2) At 500 °C, the pure-fatigue crack propagates steadily until breakage. However, the dwell-fatigue crack does not propagate continuously, which mainly relates to the blunting of the crack tip by large plastic deformation during the dwell time.
(3) The effect of pores on the fracture mechanism of SLM AlSi10Mg alloy was revealed under dwell-fatigue at 500 °C. Owing to the good toughness of the SLM AlSi10Mg alloy, there is large elongation and rotation under the joint action of normal stress and shear stress. When a dwell time is introduced, the formation of creep micropores accelerates the fracture of materials.
(4) The CPFE results show that high local plastic strain accumulating around the notch directly causes microcrack nucleation at these locations, but increasing the dwell time does not linearly affect the maximum GND density, stored energy and maximum plastic strain.

Acknowledgements This work was financially supported by the National Natural Science Foundation of China (Grant Numbers 11632010, 11872035 and 12172190).

Funding Funding was provided by National Natural Science Foundation of China (Grant Numbers 11632010, 11872035, 12172190).

References

Aboulkhair NT, Everitt NM, Ashcroft I, Tuck C (2014) Reducing porosity in AlSi10Mg parts processed by selective laser melting. Addit Manuf 1:77–86

Anand L, Kothari M (1996) A computational procedure for rate-independent crystal plasticity. J Mech Phys Solids 44 (4):525–558

Arsenlis A, Parks D (1999) Crystallographic aspects of geometrically-necessary and statistically-stored dislocation density. Acta Mater 47(5):1597–1611

Asaro RJ (1983) Micromechanics of crystals and polycrystals. Adv Appl Mech 23:1–115

Bao J, Wu S, Withers PJ, Wu Z, Li F, Fu Y, Sun W (2020) Defect evolution during high temperature tension-tension fatigue of SLM AISi10Mg alloy by synchrotron tomography. Mater Sci Eng A 792:139809

Bao J, Wu Z, Wu S, Withers PJ, Li F, Ahmed S, Benaarbia A, Sun W (2021) Hot dwell-fatigue behaviour of additively manufactured AlSi10Mg alloy: relaxation, cyclic softening and fracture mechanisms. Int J Fatigue 151:106408

Brandl E, Heckenberger U, Holzinger V, Buchbinder D (2012) Additive manufactured AlSi10Mg samples using selective laser melting (SLM): microstructure, high cycle fatigue, and fracture behavior. Mater Des 34:159–169

Busso E, Meissonnier F, O'dowd N, (2000) Gradient-dependent deformation of two-phase single crystals. J Mech Phys Solids 48(11):2333–2361

Chen X, Yang Z, Sokolov MA, Erdman DL III, Mo K, Stubbins JF (2013) Low cycle fatigue and creep-fatigue behavior of Ni-based alloy 230 at 850° C. Mater Sci Eng A 563:152–162

Chen B, Jiang J, Dunne FP (2018) Is stored energy density the primary meso-scale mechanistic driver for fatigue crack nucleation? Int J Plast 101:213–229

Cottrell AH (1953) Dislocations and plastic flow in crystals.

Ding B, Ren W, Peng J, Zhong Y, Li F, Yu J, Ren Z (2018) Revealing the creep-fatigue deformation mechanism for a directionally-solidified Ni-based superalloy DZ445 at 900° C. Materials Research Express 5(7):076513

Dunne F, Rugg D, Walker A (2007a) Lengthscale-dependent, elastically anisotropic, physically-based hcp crystal plasticity: application to cold-dwell-fatigue in Ti alloys. Int J Plast 23(6):1061–1083

Dunne F, Wilkinson A, Allen R (2007b) Experimental and computational studies of low cycle fatigue crack nucleation in a polycrystal. Int J Plast 23(2):273–295

Dunne F, Kiwanuka R, Wilkinson A (2012a) Crystal plasticity analysis of micro-deformation, lattice rotation and geometrically necessary dislocation density. Proc R Soc A 468(2145):2509–2531

Dunne F, Kiwanuka R, Wilkinson A (2012b) Crystal plasticity analysis of micro-deformation, lattice rotation and geometrically necessary dislocation density. Proc R Soc A 468(2145):2509–2531

Dunne F, Kiwanuka R, Wilkinson A (2012c) Crystal plasticity analysis of micro-deformation, lattice rotation and geometrically necessary dislocation density. In: Proceedings of Royal Society A, vol 2145, pp 2509–2531. The Royal Society

Dursun T, Soutis C (2014) Recent developments in advanced aircraft aluminium alloys. Mater Des 1980–2015 (56):862–871

Everaerts J, Gontcharov D, Verlinden B, Wevers M (2017) The influence of load holds on the fatigue behaviour of drawn Ti-6Al-4V wires. Int J Fatigue 98:203–211

Gibbs G (1969) Thermodynamic analysis of dislocation glide controlled by dispersed local obstacles. Mater Sci Eng 4 (6):313–328

Granato A, Lücke K, Schlipf J, Teutonico L (1964) Entropy factors for thermally activated unpinning of dislocations. J Appl Phys 35(9):2732–2745

Han C-S, Gao H, Huang Y, Nix WD (2005) Mechanism-based strain gradient crystal plasticity—I. Theory. J Mech Phys Solids 53(5):1188–1203

Hu D, Ma Q, Shang L, Gao Y, Wang R (2016) Creep-fatigue behavior of turbine disc of superalloy GH720Li at 650 C and probabilistic creep-fatigue modeling. Mater Sci Eng A 670:17–25

Jiang J, Yang J, Zhang T, Zou J, Wang Y, Dunne F, Britton T (2016) Microstructurally sensitive crack nucleation around inclusions in powder metallurgy nickel-based superalloys. Acta Mater 117:333–344

Kanvinde A, Deierlein G (2007) Cyclic void growth model to assess ductile fracture initiation in structural steels due to ultra low cycle fatigue. J Eng Mech 133(6):701–712

Korsunsky AM, Dini D, Dunne FP, Walsh MJ (2007) Comparative assessment of dissipated energy and other fatigue criteria. Int J Fatigue 29(9–11):1990–1995

Kundu T (2012) Ultrasonic and electromagnetic NDE for structure and material characterization: engineering and biomedical applications. CRC Press

Kysar J, Saito Y, Oztop M, Lee D, Huh W (2010) Experimental lower bounds on geometrically necessary dislocation density. Int J Plast 26(8):1097–1123

Lee EH (1969) Elastic-plastic deformation at finite strains. J Appl Mech 36(1):1–6

Li P, Kim Y, Bobel A, Hector L Jr, Sachdev A, Kumar S, Bower A (2021) Microstructural origin of the anisotropic flow stress of laser powder bed fused AlSi10Mg. Acta Mater 220:117346

Liu A, Chua CK, Leong KF (2010) Properties of test coupons fabricated by selective laser melting. Key Engineering Materials. Trans Tech Publ, pp 780–784

Maamoun AH, Elbestawi M, Dosbaeva GK, Veldhuis SC (2018) Thermal post-processing of AlSi10Mg parts produced by selective laser melting using recycled powder. Addit Manuf 21:234–247

Manonukul A, Dunne F (2004) High–and low–cycle fatigue crack initiation using polycrystal plasticity. In: Proceedings of the Royal Society of London A, vol 2047, pp 1881–1903. The Royal Society

McGinty R, McDowell D (2006) A semi-implicit integration scheme for rate independent finite crystal plasticity. Int J Plast 22(6):996–1025

Michi RA, Plotkowski A, Shyam A, Dehoff RR, Babu SS (2021) Towards high-temperature applications of aluminium alloys enabled by additive manufacturing. Int Mater Rev 1–48

Paoletti C, Cerri E, Ghio E, Santecchia E, Cabibbo M, Spigarelli S (2021) Effect of low-temperature annealing on creep properties of AlSi10Mg alloy produced by additive manufacturing: experiments and modeling. Metals 11 (2):179

Read N, Wang W, Essa K, Attallah MM (2015) Selective laser melting of AlSi10Mg alloy: process optimisation and mechanical properties development. Mater Des 1980–2015(65):417–424

Schneller W, Leitner M, Springer S, Grün F, Taschauer M (2019) Effect of HIP treatment on microstructure and fatigue strength of selectively laser melted AlSi10Mg. J Manuf Mater Process 3(1):16

Suresh S (1998) Fatigue of materials. Cambridge University Press

Tang M, Pistorius PC (2017) Oxides, porosity and fatigue performance of AlSi10Mg parts produced by selective laser melting. Int J Fatigue 94:192–201

Tang M, Pistorius PC (2019) Fatigue life prediction for AlSi10Mg components produced by selective laser melting. Int J Fatigue 125:479–490

Taylor GI (1934) The mechanism of plastic deformation of crystals. Part I. Theoretical Proc R Soc Lond A 145 (855):362–387

Uzan NE, Shneck R, Yeheskel O, Frage N (2018) High-temperature mechanical properties of AlSi10Mg specimens fabricated by additive manufacturing using selective laser melting technologies (AM-SLM). Addit Manuf 24:257–263

Wan V, MacLachlan D, Dunne F (2014) A stored energy criterion for fatigue crack nucleation in polycrystals. Int J Fatigue 68:90–102

Wang Z, Wu W, Qian G, Sun L, Li X, Correia JA (2019) In-situ SEM investigation on fatigue behaviors of additive manufactured Al-Si10-Mg alloy at elevated temperature. Eng Fract Mech 214:149–163

Wang Z, Wu W, Liang J, Li X (2020) Creep-fatigue interaction behavior of nickel-based single crystal superalloy at high temperature by in-situ SEM observation. Int J Fatigue 141:105879

Wilson D, Zheng Z, Dunne FP (2018) A microstructure-sensitive driving force for crack growth. J Mech Phys Solids 121:147–174

Wu H, Li J, Wei Z, Wei P (2020) Effect of processing parameters on forming defects during selective laser melting of AlSi10Mg powder. Rapid Prototyp J

Xu Z, Liu A, Wang X (2021) Fatigue performance and crack propagation behavior of selective laser melted AlSi10Mg in 0°, 15°, 45° and 90° building directions. Mater Sci Eng A 812:141141

Yan Q, Song B, Shi Y (2020) Comparative study of performance comparison of AlSi10Mg alloy prepared by selective laser melting and casting. J Mater Sci Technol 41:199–208

Zhang T, Collins DM, Dunne FP, Shollock BA (2014) Crystal plasticity and high-resolution electron backscatter diffraction analysis of full-field polycrystal Ni superalloy strains and rotations under thermal loading. Acta Mater 80:25–38

Zhang C, Zhu H, Liao H, Cheng Y, Hu Z, Zeng X (2018) Effect of heat treatments on fatigue property of selective laser melting AlSi10Mg. Int J Fatigue 116:513–522

Zhao L, Macías JGS, Ding L, Idrissi H, Simar A (2019) Damage mechanisms in selective laser melted AlSi10Mg under as built and different post-treatment conditions. Mater Sci Eng A 764:138210

Zheng Z, Balint DS, Dunne FP (2016) Dwell-fatigue in two Ti alloys: an integrated crystal plasticity and discrete dislocation study. J Mech Phys Solids 96:411–427

Zrník J, Semeňák J, Vrchovinský V, Wangyao P (2001) Influence of hold period on creep-fatigue deformation behaviour of nickel base superalloy. Mater Sci Eng A 319:637–642